Scientific Reports

https://doi.org/10.1038/s41598-026-40113-5

Article in Press

Genomic and structural elucidation of multi-heavy metal tolerance in the *p*-nitrophenol-degrading bacterium *Pseudomonas asiatica* strain PNPG3

Received: 23 November 2025

Accepted: 10 February 2026

Published online: 15 February 2026

Cite this article as: Alam S.A., Karmakar D., Nayek T. *et al.* Genomic and structural elucidation of multi-heavy metal tolerance in the *p*-nitrophenol-degrading bacterium *Pseudomonas asiatica* strain PNPG3. *Sci Rep* (2026). https://doi.org/10.1038/s41598-026-40113-5

Sk Aftabul Alam, Debabrata Karmakar, Trisha Nayek, Rajkumar Mandal, Satyabrata Bhattacharya & Pradipta Saha

Genomic and structural elucidation of multi-heavy metal tolerance in the *p*-nitrophenol-degrading bacterium *Pseudomonas asiatica* strain PNPG3

Sk Aftabul Alam[1, 2] * Debabrata Karmakar[2], Trisha Nayek[2], Rajkumar Mandal[2], Satyabrata Bhattacharya[2], Pradipta Saha[2],

Department of Botany, Netaji Mahavidyalaya, Arambagh, Hooghly, W.B, India [1]

Department of Microbiology, The University of Burdwan, Golapbag, Burdwan, West Bengal 713104, India [2]

***Correspondence:**

Sk Aftabul Alam, PhD
Department of Botany, Netaji Mahavidyalaya, Arambagh, Hooghly, 712601, India
Phone- +91-9382005133
Email: aftabul1992@gmail.com
Orcid Id: 0000-0002-6668-4383

Abstract

Pseudomonas asiatica strain PNPG3 demonstrated broad-spectrum heavy-metal tolerance, with minimum inhibitory concentrations (MICs) of 800, 400, 4, and 6 μg/mL (ppm) for arsenite, cadmium (Cd), cobalt (Co), and nickel (Ni), respectively. When exposed to 1 mM arsenite, strain PNPG3 retained approximately 89% of its *p*-nitrophenol (PNP) degradation efficiency relative to the PNP-only baseline, mineralizing 86% of 0.5 mM PNP within 66 h and releasing 0.41 mM nitrite, indicating strong catabolic resilience under combined PNP–arsenite stress. Genome analysis identified a distinct arsenic (As) tolerance and biotransformation gene cluster on contig 1, comprising coordinated transport, regulatory, and metabolic components, including an ArsR/SmtB family transcriptional regulator and an ArsJ-associated glyceraldehyde-3-phosphate dehydrogenase, suggesting the presence of a specialized and potentially novel As detoxification mechanism. Comparative genomics further revealed conservation of key abiotic and biotic stress response genes, along with metabolic pathways supporting degradation of styrene, dioxins, polycyclic aromatic hydrocarbons, cyanate, and diverse aromatic xenobiotics.

Chromate reductase (ChrR) and arsenate reductase (ArsC), key enzymes involved in the biotransformation of Cr (VI) to Cr (III) and arsenate [As(V)] to arsenite [As(III)], respectively, were modeled, characterized, and validated, followed by docking analyses to elucidate heavy-metal interactions at their active sites. Molecular dynamics simulation (MDS) indicated that the ArsC–arsenate complex exhibited higher structural stability and compactness, with limited conformational fluctuations, implied greater robustness of arsenate reduction compared to Cr(VI) reduction under *in situ* metal stress conditions.

Overall, the phenotypic robustness and genomic potential of strain PNPG3 underscore its strong capacity for heavy-metal tolerance, PNP biodegradation, and arsenate biotransformation, highlighting its promise for scalable bioremediation applications.

Introduction

The proliferation of anthropogenic activities has intensified the discharge of a wide range of environmental contaminants, significantly exacerbating global pollution across terrestrial and aquatic ecosystems. Among these pollutants, *p*-nitrophenol (PNP) has garnered considerable attention due to its persistence, toxicity, and widespread industrial applications. It is extensively employed in the production of dyes, petrochemicals, pharmaceuticals, pesticides, explosives, and leather goods, thereby facilitating its release into the environment through industrial effluents[42]. Within the agricultural systems, PNP often arises as a major degradation product of organophosphate pesticides through hydrolytic and oxidative processes[26]. PNP functions as an uncoupler of oxidative phosphorylation, disrupting cellular respiration and energy transduction pathways[39]. Moreover, its mutagenic and carcinogenic potential, documented in both humans and model organisms, has led to its classification as a priority pollutant by regulatory agencies worldwide[36]. Due to its biochemical recalcitrance, conventional remediation approaches are often ineffective. Physicochemical techniques such as adsorption, chemical oxidation, photodegradation, and electrochemical treatments are also frequently cost-prohibitive, particularly for large-scales[20]. Consequently, bioremediation, particularly the microbial degradation of PNP, has emerged as a sustainable, eco-friendly, and

economically viable alternative[38]. Notably, *Pseudomonas asiatica* strain PNPG3, isolated from the river Ganges, exhibits exceptional PNP degradation potential, utilizing the compound as a sole carbon source[4]. This strain demonstrated optimal growth at 0.5 mM PNP concentration and tolerated levels up to 6 mM, the highest reported to date for any PNP-degrading organism. Additionally, strain PNPG3 exhibited chemotactic responses toward structurally related xenobiotics, including *p*-benzoquinone and 4-aminophenol. This behavior highlights its adaptive ecological role in pollutant-rich environments[5]. Such findings underscore the ability of strain PNPG3, inhabiting contaminated niches to evolve specialized metabolic pathways capable of mineralizing recalcitrant organic contaminants.

Parallel to organic pollutants, heavy metal contamination represents a major ecological challenge. Industrial processes such as smelting, mining, electroplating, and manufacturing, along with diffuse sources like corroded pipelines and urban runoff, contribute substantially to the accumulation of trace metals in soil and aquatic systems[1]. Metals such as zinc, copper, iron, and manganese serve as essential micronutrients, functioning as enzymatic and redox cofactors. However, elevated concentrations disrupt normal physiological processes. Excess metal accumulation induces oxidative stress, protein denaturation, enzyme inhibition, and damage to cellular structures in microorganisms, plants, and higher organisms[21]. Heavy metals such as As, chromium (Cr), Cd, copper, mercury, and lead (Pd) exhibit pronounced cytotoxic, carcinogenic, and mutagenic effects, even at trace concentrations[2]. Arsenite is released into the environment through a range of natural and anthropogenic processes. In its trivalent form, arsenite (AsO_2^-) readily interacts with sulfhydryl groups of proteins and dithiols, leading to pronounced cellular toxicity. In contrast, the pentavalent species arsenate (AsO_4^{3-}) is comparatively less toxic and acts as a structural analogue of phosphate, forming arsenylated intermediates that disrupt phosphorylation pathways. The permissible concentration of As in drinking water is 0.01 ppm[2]. Cr, particularly Cr(VI), is classified as a group 1 carcinogen and induces carcinogenesis through multiple, interrelated molecular mechanisms. These include the generation of elevated oxidative stress, chromosomal aberrations, and formation of DNA adducts, all of which contribute significantly to genomic instability[17]. Previous studies have demonstrated that Cd exposure has been associated with an increased risk of several malignancies, including cancers of the prostate, breast, nasopharynx, lung, pancreas, and kidney[19]. Over time, this results in detrimental bioaccumulation and biomagnification through food webs, posing serious ecological and health risks. Thus, the co-occurrence of arsenic, cadmium, cobalt, and chromium alongside phenolic xenobiotics is hypothesized to severely compromise ecosystem integrity and environmental sustainability.

The simultaneous presence of PNP, and toxic heavy metals in contaminated sites imposes severe environmental stress, posing significant challenges to remediation strategies. Despite extensive work on PNP-degrading bacteria, little is known about strains that can simultaneously degrading PNP while tolerating high concentrations of arsenic and other heavy metals in mixed-waste environments. Addressing such complex, co-contamination scenarios requires microbial strains that combine robust xenobiotic degradation capacity with enhanced metal resistance. Accordingly, the present study investigated whether strain PNPG3 possesses intrinsic heavy metal tolerance, a trait that could substantially enhance its bioremediation potential in mixed-waste environments.

This study investigated the phenotypic heavy-metal tolerance of *Pseudomonas asiatica* strain PNPG3 and its PNP degradation capacity under arsenite stress, coupled with genome-wide identification of resistance determinants and xenobiotic metabolic pathways. Comparative genomic analyses within the genus *Pseudomonas* were conducted to contextualize these traits. Finally, structural and molecular dynamics analyses of arsenate and chromate reductases were performed to elucidate arsenic and Cr(VI) biotransformation mechanisms. Collectively, these characteristics explain the adaptability of strain PNPG3 to contaminated environments and highlight its strong potential for application in complex mixed-waste bioremediation.

Materials and Methods

Chemicals

All heavy metals and culture media used in this study were of AR grade, and were procured from Merck, HiMedia, or Sigma (≥98% purity). The solvents (methanol, ethyl acetate) employed were of HPLC grade (≥99.9% purity). Minimal media (MM), general reagents, and other chemical components were obtained from HiMedia, India.

Selection of bacterial strain and Determination of MIC of heavy metals

The strain PNPG3 was obtained through an enrichment-based isolation method[4]. The strain was cultivated in tryptone soy broth, was harvested and subsequently washed with basal minimal media (MM) (Na_2HPO_4-4.0 g; $(NH_4)_2SO_4$-0.8 g; KH_2PO_4-2.0 g; $MgSO_4 \cdot 7H_2O$-0.8 g; trace element solution-100 µl; trace element (TE) solution: Al $(OH)_3$-0.10g, LiCl-0.05 g, KI-0.05 g, $BaCl_2 \cdot 2H_2O$-0.05 g, $MgSO_4 \cdot 7H_2O$-0.08 g, H_3BO_3-0.05 g, $CoCl_2 \cdot 6H_2O$-0.01 g, $ZnSO_4 \cdot 7H_2O$-0.10 g, $NiCl_2 \cdot 6H_2O$-0.01 g, $SnCl_2 \cdot 2H_2O$-0.05 g, $(NH_4)Mo_7O_4 \cdot 4H_2O$-0.05 g, CaSO4-0.02 g, $FeSO_4$-0.02 g, Milli-Q H_2O-100 mL; (100 µl TE solution was added to 1L of MM before autoclaving). A standardized cell suspension containing approximately 10^7 CFU/mL was prepared and used as the inoculum for subsequent growth experiments. Heavy-metal tolerance was assessed by supplementing the culture medium with various water-soluble heavy metal salts. Sodium arsenite ($NaAsO_2$), and cadmium chloride monohydrate ($CdCl_2 \cdot H_2O$) were added at concentrations ranging from 200 to 1000 µg/mL, whereas cobalt(II) chloride hexahydrate ($CoCl_2 \cdot 6H_2O$) and chromium (II) chloride hexahydrate ($CrCl_2 \cdot 6H_2O$) were incorporated at concentrations from 2 to 10 µg/mL. These concentration ranges were selected based on preliminary tolerance assays, ensuring coverage of inhibitory thresholds suitable for evaluating metal tolerance. The base medium used for these assays was sucrose low phosphate (SLP) broth, composed of 1% sucrose, 0.05% $MgSO_4 \cdot 7H_2O$, 0.01% NaCl, 0.1% $(NH_4)_2SO_4$, and 0.05% yeast extract, adjusted to pH 7.0. A cell suspension containing approximately 10^7 CFU/mL was inoculated into media with varying concentrations of heavy metals and incubated at 28 °C for 72 hours. The MIC was defined as the lowest concentration of a given toxicant that completely inhibited visible bacterial growth under defined experimental conditions after a specified incubation period. In this study, the MIC was determined as the lowest concentration at which the minimum viable cell count, as assessed by plate-based enumeration, and a corresponding reduction in optical density at 600 nm (OD_{600}) were observed[3]. All experiments were carried out using three independent biological replicates, with each biological replicate analyzed in triplicate as technical replicates.

PNP degradation in presence of arsenite

Cells were grown in TSB, harvested by centrifugation, washed twice with MM, and subsequently used for biodegradation and nitrite release assays. Biodegradation experiments were performed in 100 mL Erlenmeyer flask containing 25 mL of MM supplemented with 0.5 mM PNP in the presence of sodium arsenite (1 mM) under optimized conditions were evaluated through a PNP depletion assay. Cultures were incubated at 28 °C with shaking at 120 rpm for up to 72 h. At 12h time intervals, 1 mL aliquots were withdrawn, centrifuged at 10,000 × g for 10 min, and the supernatants were used for residual PNP estimation. In the arsenite-amended experiments, abiotic controls containing PNP and sodium arsenite without bacterial inoculation showed no measurable change in absorbance at 410 nm over the incubation period, indicating negligible spectral interference by arsenite under the experimental conditions. Accordingly, residual PNP was quantified spectrophotometrically at 410 nm as described previously[6]. Statistical comparisons between metal-free and arsenite-amended conditions were performed to evaluate differences in the percentage of PNP biodegradation over the incubation time. The statistical significance of the observed differences was assessed using an unpaired Student's t-test. Concurrently, nitrite production was quantified at regular intervals using the colorimetric method of White et al.[45]. Formation of a purple-colored complex indicated the presence of nitrite, and absorbance was measured at 540 nm against a standard curve prepared with sodium nitrite ($NaNO_2$). Quantification was performed based on a $NaNO_2$ calibration curve generated over a linear concentration range of 0.01–0.20 mM (0.01, 0.05, 0.10, 0.15, and 0.20 mM). A control setup, lacking bacterial inoculum, was maintained under identical experimental conditions.

Genome sequence and annotation

The draft genome of the selected strain was sequenced using the Illumina HiSeq X platform with a read length of 151 bp. De novo genome assembly was performed using the metaSPAdes assembler v3.11.1[34]. The assembled contigs were subsequently annotated through the RAST[11] and PGAP[41].

Analysis of heavy metal tolerance gene clusters/proteins

The presence of heavy metal tolerance gene clusters and associated proteins were confirmed using the PGAP and RAST annotation platforms and verified by BLASTX tool[8]. Heavy-metal tolerance genes in strain PNPG3 were manually curated and compared with those of *Pseudomonas* sp. PNP (JAGKJH000000000), *P.* sp. 13159349 (CP045553), *P.* sp. WBC-3 (CP142110) and *P* sp. JS425 (CP073661) to identify homologous gene counterparts. The PGPg_finder pipeline was employed to analyze and compare to these genomes with respect to their heavy metal tolerance, heavy metal resistance, stress tolerance, and xenobiotic degradation potentials, utilizing the Plant-associated Bacteria database (PLaBAse) as described by *Pellegrinetti et al.*[35].

Three-Dimensional model generation of ChrR, ArsC,

The arsenate reductase (ArsC) and chromate reductase (ChrR) sequences from strain PNPG3 were chosen for 3D structural model generation. The structural and physicochemical properties, including molecular weight, theoretical isoelectric point (pI), amino acid composition, instability index, aliphatic index, and grand average of hydropathicity

(GRAVY), of the target proteins were evaluated using the ProtParam module of the ExPASy platform[9]. The predictions of secondary structural components (α-helices, β-strands, turns, and random coils) were carried out using the SOPMA server[18] and NetSurfP-2.0[25]. Three-dimensional models of the target proteins were generated using the SWISS-MODEL workspace[10]. To assess the structural quality and reliability of the generated models, comprehensive validation analysis were performed. The models were evaluated using ERRAT[15] and PROCHECK[27] programs available through the SAVES v6.0 server, along with additional quality assessment using the QMEAN4 server (https://swissmodel.expasy.org/qmean/) to examine stereochemical integrity and overall model quality. The .pdb files generated by SWISS-MODEL were subsequently analyzed to construct Ramachandran plots via the SAVES server.

In silico prediction of active site and molecular docking analysis of ligands with target proteins

The active site of the target proteins were predicted using the PrankWeb server[22], which employs machine learning–based algorithms to identify potential binding sites. The 2D structures of arsenate, arsenite, Cr(VI)carbonate, and Cr(VI) oxalate ions were obtained from the PubChem database and downloaded in SDF format for subsequent analysis. The CB-Dock2 server was employed to predict potential ligand-binding sites and to perform molecular docking of the selected ligands with the target proteins[30]. Binding pockets were identified using the curvature-based cavity detection algorithm implemented in CB-Dock2, and grid box center coordinates and dimensions were automatically generated to fully encompass each predicted cavity. Docking simulations were carried out using the integrated AutoDock Vina engine, with default exhaustiveness and scoring parameters, and no additional positional or interaction constraints were applied. Among the predicted docking poses, the complex exhibiting the lowest binding energy (Vina score) was considered the most stable and was selected for further structural and interaction analyses. Finally, the molecular interactions between the receptor and the ligand complex were analyzed and visualized using ligplot plus tool[28]. This analysis provided detailed insights into the binding orientation, interaction types, and stability of the docked complexes, thereby enhancing the understanding of the molecular basis of ligand–receptor affinity observed in the docking results.

MDS

MDS were performed using the GROMACS 2024.1 package with the CHARMM27 force field. A time step of 2 fs was used for all simulations. Long-range electrostatic interactions were calculated using the Particle Mesh Ewald (PME) method with a real-space cutoff of 1.0 nm, while van der Waals interactions were truncated at 1.0 nm. The objective was to investigate the structural stability and dynamic properties of the docked complexes formed between arsenate and Cr(VI) oxalate with the ArsC and ChrR proteins derived from strain PNPG3. Each system was solvated using the SPC water model, following the protocol described by Wu et al.[46]. To maintain electrostatic neutrality, Na^+ and Cl^- ions were incorporated by replacing selected water molecules. After energy minimization, the system was equilibrated in two successive phases: the NVT (constant Number of particles, Volume, and Temperature) ensemble followed by the NPT (constant Number of particles, Pressure,

and Temperature) ensemble, each conducted for 100 ps. Temperature and pressure were maintained using the V-rescale thermostat and Parrinello–Rahman barostat, respectively. Once equilibrium was achieved, a 100 ns production run was carried out under constant temperature (300 K) and pressure (1 atm) conditions. Production simulations were carried out for the indicated time scale without any restraints.

To evaluate structural stability and conformational changes of each complex during molecular dynamics simulations, root mean square deviation (RMSD), radius of gyration (Rg), root mean square fluctuation (RMSF), solvent-accessible surface area (SASA), and intermolecular hydrogen-bond analyses were performed throughout the simulation. All analyses were executed using the integrated utilities of the GROMACS software suite, while graphical representations were generated using XMGrace, ensuring a thorough evaluation of the system's structural dynamics.

PCA

Principal Component Analysis (PCA) was employed to examine the covariance matrices of the positional fluctuations of Cα atoms, offering a quantitative framework for understanding the dynamic behavior of proteins[16]. Visualization of the dynamic modes was performed using XMGrace. Owing to the highly correlated and collective nature of the protein motions, a limited number of principal components, particularly PC1 and PC2 were sufficient to capture the predominant conformational variations observed throughout the simulation.

Results and Discussion

Heavy metal tolerance assay

The bacterial strain PNPG3 was isolated from the river Ganges in W.B, India. The sampling site was located near several pharmaceutical, petrochemical manufacturing units that contribute to heavy metal contamination of the surrounding soils. Isolation of strain PNPG3 from this environment suggests its adaptive capability to tolerate and survive under elevated concentrations of metal ions. The strain was evaluated across a broad concentration range, with As and Cd tested up to 1000 ppm and Co and Cr up to 10 ppm. The strain exhibited remarkable tolerance to multiple heavy metals, demonstrating the ability to withstand concentrations of up to 800 ppm arsenite, 400 ppm Cd, 4 ppm Co, and 6 ppm Cr (Figure 1A-D); Supplementary Figure 1A-D. Collectively, these results indicate that although the strain displays substantial resistance to multiple heavy metals, its tolerance is concentration-dependent, with clear inhibitory effects observed at higher metal loads. Importantly, MIC values were highly consistent across independent biological replicates, with minimal inter-replicate variation (± SD < 5%), indicating stable and reproducible metal tolerance phenotypes. This pattern clearly demonstrates metal-specific toxicity, characterized by exceptionally high resistance to As and Cd but comparatively lower tolerance to cobalt and chromium. The pronounced arsenite resistance of strain PNPG3 is particularly relevant in the context of arsenic-rich sediments of the Ganges basin, where arsenic contamination is widespread and represents a major environmental and public health concern. The ability of PNPG3 to survive under elevated arsenic concentrations suggestes that it is well adapted to real-world co-contaminated environments rather than laboratory-optimized conditions alone. Sengupta et al. previously reported that the PNP degrading bacterium *Bacillus* sp. strain BUPNP2 exhibited tolerance to several heavy metals, including Cr, iron, Pb, Cd, Ni, and zinc

under both catabolic and co-metabolic conditions[37]. Among the metals evaluated, Fe and Ni imposed comparatively lower inhibitory effects on PNP degradation by strain BUPNP2. In contrast, Cd and Pb exerted the most pronounced inhibitory influence, resulting in substantially reduced PNP degradation. *Enterococcus gallinarum* strain JT-02, has been reported to biodegrade PNP. In addition, this strain has also been reported to effectively bioremediate hexavalent chromium [Cr(VI)] and to exhibiting tolerance to multiple heavy metals, including Cu^{2+}, Ni^{2+}, Co^{2+}, Pb^{2+}, and Zn^{2+}[(43)]. To the best of the authors' knowledge, no previous studies have explicitly reported a *Pseudomonas* strain that both degrades PNP and has been experimentally demonstrated to tolerate heavy metal stress during biodegradation.

PNP degradation in presence of arsenite

The bacterial strain PNPG3 demonstrated effective catabolic utilization of PNP in presence of heavy metal arsenite. When exposed to 1 mM arsenite, the strain efficiently degraded approximately 86% of 0.5 mM PNP within 66 hours, accompanied by the release of nitrite. During complete mineralization of PNP, the strain liberated 0.41 mM nitrite over the same time period (Figure 2A, B). The observed cellular growth in PNP-heavy metal supplemented medium, together with the parallel decline in PNP concentration and accumulation of nitrite, clearly suggests that transformation of the parent compound was involved in the degradation pathway. While the concentration of 1 mM arsenite used in this study exceeds the average dissolved arsenic levels typically reported in the Ganges River basin, elevated arsenic concentrations have been documented in regional groundwater (up to 4,730 µg/L) and irrigation water (~1,000 µg/L)[14]. The 1 mM arsenite concentration was therefore selected to elicit a robust and clearly observable physiological stress response. In the context of the Ganges basin, this concentration serves as an accelerated model of acute toxicity, enabling characterization of specific metabolic pathways that may be more subtly affected under chronic exposure to lower, environmentally relevant doses.

Previous investigations on strain PNPG3 demonstrated its high efficiency in the catabolic degradation of PNP, achieving approximately 97% degradation within 60 hours, accompanied by the release of 0.44 mM nitrite[4]. The unpaired Student's t-test revealed a highly significant difference in PNP biodegradation between the compared conditions, with a p-value < 0.00001, indicating statistical significance well below the 0.01 threshold. The present findings demonstrated that the strain maintained its PNP biodegradation capability even in the presence of arsenic stress, although the rate of PNP utilization was comparatively reduced. This resilience may be attributed to the presence of a ~9.3 kb genomic region in strain PNPG3 harbored the *pdcABC1C2DEFG* gene cluster, which was responsible for conferring the PNP biodegradation phenotype[4]. This reduced efficiency suggests that the heavy-metal stress may influence the kinetics of the catabolic pathway.

Notably, the ability of PNPG3 to continue degrading PNP under such conditions highlighted a robust and adaptable metabolic system. It is plausible that specific catabolic genes or regulatory elements within PNPG3 become activated or upregulated in response to heavy-metal exposure, enabling the organism to maintain its biodegradative function despite environmental stress. This adaptive response underscores the strain's potential for bioremediation applications in complex, co-contaminated environments where both xenobiotics and heavy metals coexist. Interestingly, earlier studies revealed that the

degradation of PNP by strain PNPG3 proceeded via the formation of *p*-benzoquinone and 1,2,4-benzenetriol as key intermediates[4].

Heavy metal tolerance gene annotation of strain PNPG3

Bioinformatics analysis conducted using the PGAP server identified a comprehensive set of heavy metal tolerance genes in strain PNPG3. The genome harbors twelve As resistance genes, including *arsB*, *arsJ*, *arsC*, *arsR*, and *arsH*; three Cd resistance-associated genes, namely *cadR*, *cadA*, and *clpB*; two genes encoding CusA/CzcA family heavy metal efflux RND transporters; two Cr resistance genes (*chrA* and *chrR*); and two Co resistance genes (*rcnB* and related loci). Additionally, several genes encoding heat shock protein families such as Hsp33, Hsp20, and Hsp70 were also detected. In total, thirty-seven proteins were found to contribute to the heavy metal tolerance mechanisms of strain PNPG3 (Table 1).

The *arsH* gene (locus tag: MJ643_01565, accession: JALLKV010000001) in strain PNPG3 was 716 nucleotides in length and encoded a protein that shows 100% amino acid sequence identity to the ArsH protein of *Pseudomonas* (accession number WP_208209232.1). Similarly, the *cadA* gene, encoding a Cd-translocating P-type ATPase (locus tag: MJ643_17445; accession: JALLKV010000025), showed complete (100%) amino acid sequence homology with the CadA protein of *Pseudomonas* sp. (WP_024087433.1). A comprehensive summary of the homologous heavy metal tolerance genes identified in *P. asiatica* strain PNPG3 is presented in Table 1.

The *arsR* gene encoded a transcriptional repressor belonging to the SmtB/ArsR family of metalloregulatory proteins. The *arsB* component functions as an efflux pump capable of forming an independent ATP-dependent arsenite [As(III)] export system, facilitating the exclusion of arsenite from the cell. Additionally, the *arsC* gene encoded the canonical prokaryotic arsenate [As(V)] reductase, (ArsC), which catalyzed the reduction of arsenate to arsenite[44]. *CzcA* functions as a H^+ antiporter and an ATPase, playing a pivotal role in conferring resistance to heavy metals such as Cd and Co in various Gram-negative bacteria[24]. Moreover, *clpB* and *cadA* (the P-type ATPase) have been reported to play crucial roles in Cd resistance[24,32]. Chromate reductase (ChrR) is employed in bioremediation processes to eliminate chromate contaminants from the environment by catalyzing the reduction of the toxic hexavalent chromium [Cr(VI)] to its less toxic trivalent form [Cr(III)][40]. A survey of the literature revealed that bacteria possess specialized proteins such as Hsp70 that enable them to withstand stress conditions and contribute to the detoxification or removal of heavy metals[31].

Genome analysis revealed the presence of an As tolerance gene cluster located on contig 1 (JALLKV010000001) (Figure 3A). This cluster comprises a single copy each of *arsB, arsH, ars*J, a metalloregulatory a*rsR/smtB* family transcription factor, and an *arsJ*-associated glyceraldehyde-3-phosphate dehydrogenase (GADPH), collectively contributing to the strain's potential mechanism of As detoxification and resistance, as supported by Yan et al. [47] (Figure 3A). Although many bacteria—such as *Staphylococcus xylosus* pSX267, *S. aureus* PI258, *Escherichia coli* Chr, *Pseudomonas aeruginosa* pKW301, and *P. fluorescens* Chr—commonly harbor the canonical *arsRBC* operon, and variants such as *arsCRBH*, *arsCBRH* and *arsRB* have been documented in *Thiobacillus ferrooxidans* Chr, *Yersinia* pYV and *Ferroplasma acidarmanus Chr* respectively[12, 13, 23,33] the genomic organization in strain PNPG3 was notably different (Figure 3-B,C,D,E). This strain features an *arsRBHJ* gene

arrangement with GADPH gene, representing an atypical configuration that may reflect a distinct evolutionary trajectory or functional specialization in As resistance. To the best of authors' knowledge, presence of this unique ars gene cluster likely underlies the high arsenite MIC and the sustained PNP degradation observed under arsenic stress.

Prokaryotic genomes commonly harbor several *ars* genes with overlapping or complementary functions, a genomic architecture that is frequently associated with elevated resistance to diverse As species. This multiplicity is thought to reflect a long evolutionary history shaped by persistent exposure to As-rich niches[29]. Early evolutionary models suggest that ancestral *arsRB* operons originated in predominantly anaerobic environments, where arsenite was likely the principal bioavailable arsenic species. These primitive operons were compact, encoded only essential regulatory and efflux components (ArsR and ArsB), which conferred a selective advantage under high arsenite stress. Over time, the *ars* system diversified through gene duplication and horizontal gene transfer, resulting in the expansion and functional redundancy of *ars* genes that enhanced arsenic detoxification capacity and adaptive flexibility in arsenic-impacted environments.

In classical *arsRBC* systems, *arsC* was coupled to arsenite efflux via *arsB*, providing a linear detoxification route primarily focused on arsenic extrusion. In contrast, the PNPG3 cluster lacks *arsC* within the operon but incorporates *arsH*, implicated in arsenite detoxification and protection against arsenic-induced oxidative stress, thereby expanding the functional scope beyond simple efflux. The presence of *arsJ* and an adjacent GAPDH suggests an alternative arsenate resistance mechanism involving arsenylated sugar-phosphate intermediates, enabling arsenate detoxification through metabolic bypass pathways. This mechanism effectively 'bypasses' the toxic intracellular reduction step, potentially minimizes oxidative damage and metabolic burden, a hypothesis supported by the co-localization of the *arsH* gene and stress-response modules (*hsp70*, *hsp33*) within the PNPG3 genome. Collectively, this atypical operon architecture likely confers greater metabolic flexibility and resilience under arsenic stress compared to canonical *arsRBC* or *arsCRBH* operons, allowing sustained cellular metabolism and catabolic activity under elevated arsenite exposure.

Comparative analysis of the heavy metal tolerance repertoire of strain PNPG3 with those of *Pseudomonas* sp. 13159349, *Pseudomonas* sp. JS425, *Pseudomonas putida* WBC-3, and *Pseudomonas alloputida* PNP revealed notable differences in gene content. Among the reference strains, several lacked key determinants such as *arsH*, which was present only in PNPG3. Variation was also observed in the copy number of *cadA*: strains JS425 and PNP possessed three paralogs of this Cd translocating ATPase, whereas strains 13159349 and WBC-3 did not encode this gene. A similar pattern emerged for the CzcA efflux transporter, which was absent from strains 13159349, JS425, and WBC-3 but occurred in duplicate in strain PNP. A consolidated overview of these heavy metal tolerance genes across the compared genomes is presented in Table 2.

The presence of multiple heavy metal tolerance genes, including *arsC, cadR, cadA, clpB, chrA, chrR, hsp70,* and *hsp33*, within the genome of strain PNPG3 suggests an enhanced genetic capacity for detection and response to heavy metal stress in subsurface environments. This genomic repertoire plausibly reflects the strain's adaptive mechanism to persist and thrive under metal-contaminated ecological conditions. The comparatively slower PNP degradation kinetics observed under arsenite stress may be attributed to metal-induced oxidative stress and metabolic energy diversion toward detoxification processes. This interpretation is supported by the genomic enrichment of stress-response and efflux-

associated genes in strain PNPG3, including *arsB*, *cadA*, *czcA*-family transporters, and multiple heat shock proteins (*hsp20*, *hsp33*, and *hsp70*), which likely impose an energetic burden that transiently limits catabolic efficiency.

The PGPg_Finder based stress response gene heatmap (Figure 4A) revealed marked differences in stress-associated modules among the analyzed strains. Within the dendrogram, PNPG3 clustered near the center, indicative of a relatively balanced allocation of genes across multiple stress categories. This strain displayed genes linked to salinity detoxification, oxidative and nitrosative stress defense, and osmotic stress regulation. In contrast to *Pseudomonas* sp. 13159349, which exhibited a notable paucity of low-temperature response genes, PNPG3 possessed moderate to high levels of both cold- and heat-tolerance determinants, reflecting enhanced thermal plasticity. PNPG3 also differed from strains WBC-3 and 13159349 in stress-signaling and biotic stress–associated pathways, where it showed comparatively lower gene enrichment.

All strains displayed comparable numbers of genes associated with abiotic stress mitigation; however, PNPG3 maintained gene counts on par with JS425, WBC-3, and PNP, indicating the preservation of essential abiotic stress tolerance mechanisms (Figure 4B). Importantly, PNPG3 recorded the highest number of genes linked to biotic stress neutralization (3.0), marginally exceeding the other strains like 13159349, JS425 and WBC-3 and implied a broader capacity to withstand antagonistic microbes or inhibitory metabolites. Although universal stress response genes were distributed fairly consistently across strains, PNPG3 again exhibited an intermediate-to-high abundance, reinforcing its robust stress adaptation profile (Figure 4B). Compared with strains 13159349 and PNP—both of which exhibited reduced gene inventories across multiple metal-resistance categories—PNPG3 maintained a more comprehensive and functionally diverse repertoire of heavy-metal resistance determinants. In particular, PNPG3 demonstrated stronger representation of genes associated with Co resistance than strains JS425, 13159349, and PNP (Figure 4C). Similarly, its antimony-resistance gene content exceeded that of strains WBC-3, PNP, and 13159349, indicating a comparatively enhanced adaptive capacity against these metal stressors (Figure 4C).

The Level-4 xenobiotic-degradation heatmap revealed substantial variation in metabolic versatility among the strains. PNPG3 harbored a wide array of catabolic modules, encompassing pathways for styrene and dioxin degradation, polycyclic aromatic hydrocarbons, plant-derived glycosidases, toluene and benzoate derivatives, cyanate utilization, aromatic-compound breakdown, and xenobiotic detoxification mediated by transport systems (Figure 4D). In contrast, strains 13159349 and JS425 displayed limited enrichment across numerous xenobiotic pathways. PNPG3, however, showed a consistently elevated baseline across most categories, underscoring the breadth and adaptability of its metabolic machinery. While PNP and JS425 exhibited strong but localized responses to specific xenobiotics, PNPG3 demonstrated a more balanced and comprehensive detoxification profile, particularly with respect to polycyclic aromatic hydrocarbon degradation. Overall, these patterns suggest that PNPG3 possesses broad xenobiotic-degradation capabilities, positioning it as a promising candidate for environmental bioremediation.

Collectively, these features position PNPG3 as one of the strains with the most uniformly distributed and functionally diverse stress-response, xenobiotic-degradation repertoires, suggesting of superior resilience to multiple environmental stressors.

Analysis of target sequences ChrR, and ArsC

Building on a comprehensive evaluation of the phenotypic and genomic characteristics of PNPG3, the arsenate reductase (ArsC) and chromate reductase (ChrR) enzymes were selected for 3D structural modeling. This choice was informed by the strain's demonstrated metabolic versatility. PNPG3 degraded the carcinogenic xenobiotic compound PNP even under heavy-metal stress and exhibited metabolism-dependent chemotaxis toward PNP, *p*-benzoquinone (PBQ), and 4-aminophenol (4AP)[5]. The strain was isolated from the polluted waters of the river Ganges[4] and has shown substantial tolerance to multiple metals, indicating its capacity to participate in the biotransformation and detoxification of toxic elements such as As and Cr. ChrR functions as a key detoxification enzyme by reducing hexavalent chromium [Cr(VI)], a highly toxic and mobile form, to the less harmful trivalent chromium [Cr(III)]. In parallel, ArsC catalyzes the reduction of As(V) to As(III), facilitating its subsequent efflux from the bacterial cell by ArsB. The amino acid sequences of the ArsC and ChrR were obtained from the NCBI database in FASTA format. The corresponding gene and protein accession details are as follows: *arsC* – Gene: JALLKV010000069, MCK2124297.1; Protein ID: MJ643_27390; *chrR* – Gene: JALLKV010000004, MCK2120017.1; Protein ID: MJ643_05320.

The *arsC* of strain PNPG3 spans 353 nucleotides and exhibited 100% amino acid sequence identity with the ArsC protein of *Pseudomonas* (accession no. WP_047594822.1). Similarly, the *chrR* gene encoded chromate reductase in strain PNPG3 is 560 nucleotides long and encodes a protein that shares 100% amino acid sequence identity with the ChrR protein reported in *Pseudomonas* (accession number *WP_003261018.1*) (Table 1).

Physicochemical profiling provides essential insights into the inherent structural and functional characteristics of proteins. In the present study, two target proteins were evaluated based on key biochemical parameters, including molecular weight, total amino acid content, residue composition, aliphatic index, isoelectric point (pI), and GRAVY values. A detailed summary of these properties was presented in Supplementary Table 1. Analysis using the ExPASy ProtParam server showed that leucine and alanine were the most abundant residues in ArsC (17.9%) and ChrR (12.4%), respectively, indicating their potential contribution to the overall structural integrity and stability of these proteins. Both proteins displayed notably high aliphatic index values (113.50 for ArsC and 88.66 for ChrR), reflecting strong predicted thermostability. Such stability characteristics highlight their suitability for various industrial and research applications requiring robust protein performance under elevated temperatures.

SOPMA analysis revealed that random coils constituted a substantial portion of the secondary structure in both proteins, representing 41.03% in ArsC and 45.70% in ChrR (Supplementary Figure 2A and 2C). Such a predominance of disordered regions may enhance the proteins' conformational flexibility and dynamic responsiveness. In contrast, both proteins also displayed a high proportion of α-helical elements, accounting for 45.30% in ArsC and 41.40% in ChrR, indicating the presence of stable structural motifs within their overall architecture. The NetSurf-P server predicted seven α-helices and five β-strands in ArsC, while ChrR displayed a comparable architecture with eight α-helices and eight β-strands (Supplementary Figure 2B and 2D). Overall, the secondary structure profiles indicated that α-helical elements were more abundant than other structural motifs. Since α-helices often play key roles in mediating protein–protein interactions, their greater prevalence may contribute to improved structural stability and interaction potential in both proteins.

The SWISS-MODEL server generated 3D structures for both ArsC and ChrR from strain PNPG3. ArsC was modeled using the target structure A0A059UT62.1.A, which shared 95.73% sequence identity and was derived from an AlphaFold model. Similarly, ChrR was built using the template Q88FF8.1.A, showing 94.62% sequence identity and based on an AlphaFold prediction. Model quality was evaluated through the SAVES v6.0 platform, and further validation of structural accuracy and reliability was conducted using ERRAT, PROCHECK, and QMEAN4. The corresponding validation metrics are presented in Table 3 and Figure 5 (A to F). The ERRAT scores obtained for ArsC and ChrR were 95.41 and 97.13, respectively, reflecting the high reliability and overall quality of the predicted models. As ERRAT values above 50 are generally indicative of well-validated structures, both models exhibit strong structural consistency[7]. The QMEAN4 scores for ArsC (0.92) and ChrR (–0.56) also fall within the acceptable range, as values near zero denote good model quality, while scores below –4 typically indicate poor structural reliability. Further structural validation was performed using PROCHECK. The Ramachandran plot for ArsC showed that 95.9% of residues were located in the most favored regions, with the remaining 4.1% in additionally allowed regions. ChrR demonstrated a similar distribution, with 94.3% of residues in the most favored regions and 5.7% in the additionally allowed regions. These results fall within the expected limits for high-quality protein models, confirming their structural soundness and reliability. A similar strategy for assessing and validating protein models has been reported in earlier studies by Alam and Saha, further supporting the robustness of the validation framework employed here[7].

Ligand binding site prediction and Molecular docking studies

The efficiency of ligand–receptor contacts is strongly influenced by the surface area and internal volume of the binding pockets, making these structural attributes essential considerations in molecular docking analyses. The physicochemical characteristics of a pocket are determined by the surrounding amino acid residues, which collectively define its chemical environment. The PrankWeb server predicted the active site regions for both target proteins, and the corresponding interacting residues were summarized in Table 4. For ArsC, the identified active site comprises Asn9, Arg11, Cys12, Ser13, Lys14, Leu35, Arg60, Glu63, Lys90, Arg94, and Arg107. In the case of ChrR, the predicted active site includes Ser13, Leu14, Arg15, Tyr19, Asn20, Pro79, Glu80, Tyr81, Ser116, and Pro117. These residues collectively define the putative ligand-binding environments of the respective proteins.

A comparative molecular docking analysis was conducted to evaluate the binding affinities of the selected ligands against ArsC and ChrR in the PNPG3 strain. Docking scores serve as critical indicators in virtual screening workflows, enabling the effective discrimination between unsuitable molecules and potential lead candidates. Among the ligands evaluated for ArsC, arsenate (ID: 27401) exhibited the most favorable binding free energy, with a value of –3.3 kcal/mol at the protein's active site (Figure 6A). The docked complex was stabilized through seven van der Waals interactions, primarily involving residues Thr61, Gly62, Arg60, and Arg107.

Similarly, for ChrR, the Cr(VI) oxalate complex (ID: 129636852) demonstrated the most favorable binding free energy, registering –4.1 kcal/mol at the enzyme's active site (Figure 6D). The interaction profile revealed contacts with several key residues, notably Ser13, Arg15, Asp17, Ser18, Tyr19, Asn20, Arg21, Pro79, Glu80, Tyr81, Arg83, Val115, Ser116, Pro117, Gly118, Ala119, Ile120, Gly121, Gly122, Phe123, and Ala151. Among these

interactions, six H bonds were formed between the ligand and ChrR at Ser13, Ser18, Tyr19, and Asn20, while an additional van der Waals interaction was observed at Pro117. Although four hydrogen bonds were formed in the ArsC–arsenite complex and seven hydrogen bonds were observed in the ChrR–Cr(VI)carbonate complex, their corresponding docking scores were comparatively lower, (–2.9 and –3.4 kcal/mol, respectively). The molecular docking interactions of all four ligands with ArsC and ChrR are summarized in Table 5 and depicted in Figure 6A–D. The docking results clearly demonstrate that the evaluated ligands possess appreciable binding affinities for both target proteins, ArsC and ChrR. These interactions indicate the strain's potential to mediate the biotransformation of toxic species into less harmful forms. Moreover, the overall docking score trends suggest that strain PNPG3 is well-suited for mitigating heavy-metal contamination, thereby contributing to improved environmental safety and sustainability. A comparable docking investigation by Alam et al. reported that the well-characterized PNP-degrading bacterium *Pseudomonas putida* DLL-E4 exhibited a docking score of –5.4 kcal/mol with the enzyme *p*-nitrophenol 4-monooxygenase[6].

MD simulations

MDS serves as a vital approach for elucidating the detailed structural behavior, stability, and adaptive properties of protein–metal complexes. By effectively bridging computational modeling with practical applications, MDS offers deep, atomistic-level insight into the dynamics and interactions that govern biomolecular systems. In this study, the dynamic conformational behavior of the ArsC and ChrR proteins from strain PNPG3 was thoroughly analyzed over a 100 ns MDS in the presence of arsenate and Cr(VI) oxalate, respectively. The objective was to assess the binding affinities and overall stability of the corresponding protein–ligand complexes. These two ligands were selected due to their comparatively better docking performances in the active site against their respective targets, surpassing the other screened candidates. This enabled a more meaningful evaluation of their binding affinities and the overall stability of the formed complexes.

RMSD analysis served as a key indicator of the time-dependent structural fluctuations of the ArsC and ChrR complexes. As one of the most widely employed parameters for evaluating protein dynamics, RMSD provides a quantitative measure of the stability and conformational flexibility of biomolecular systems during ligand interaction. The binding of small molecules can induce noticeable structural adjustments in the receptor, highlighting the ligand's effect on overall structural adaptability. In this study, the temporal progression of RMSD values was assessed for the ArsC–arsenate and ChrR–Cr(VI) oxalate complexes, with their corresponding average RMSD values determined to be 1.93 nm and 2.52 nm respectively (Supplementary Figure 3). RMSD analysis revealed that the ChrR–Cr(VI) oxalate complex displayed an initial phase of stabilization for approximately the first 15 ns, after which it exhibited a marked and continuous increase in deviation, characterized by a continual increase to values exceeding 6.0 nm after 50 ns. The progressive increase in RMSD indicated substantial conformational rearrangements and increased structural flexibility during the simulation. This behavior suggested weaker binding affinity or suboptimal conformational compatibility between ChrR and the Cr(VI) oxalate ligand. In contrast, the ArsC–arsenate complex maintained low and consistently stable RMSD values, indicative of minimal structural perturbations and a robust protein–ligand interaction. The ArsC–arsenate complex demonstrated substantially greater structural stability compared to the ChrR–Cr(VI) oxalate

complex. Overall, The ArsC–arsenate complex exhibited lower RMSD values, reflecting a more compact and structurally stable interaction compared with the ChrR–Cr(VI) oxalate complex.

In this study, RMS fluctuations in backbone residues were examined to understand the dynamic responses of ArsC and ChrR upon binding with heavy metals, thereby revealing localized conformational changes triggered by ligand interaction. Both complexes exhibited moderate residue fluctuations, generally ranging from 0.5 to 2 nm, with two or three pronounced peaks corresponding to regions likely positioned on the protein surface (Figure 7A). Such patterns indicated that flexible segments of the receptor backbone may contribute to binding stability or support essential functional motions. While reduced flexibility may reflect lower conformational entropy, it simultaneously favors greater binding precision.

A consistent or gradually decreasing radius of gyration (Rg) values typically reflected a stable, well-organized, and compact structural arrangement. As shown in Figure 7B, the average Rg values for the ArsC–arsenate and ChrR–Cr(VI) oxalate complexes were 1.4354 nm and 1.6430 nm, respectively. Both complexes demonstrated only minor fluctuations, indicating that their overall structural compactness was well maintained during the simulation. For the ArsC–arsenate complex, slight deviations in Rg were observed between approximately 25 and 40 ns, after which the complex stabilized with no major variations. Similarly, the ChrR–Cr(VI) oxalate complex displayed a brief fluctuation around 80 ns but remained structurally stable for the remainder of the simulation period. These observations confirmed that both complexes preserved their compact architecture and exhibited structural integrity throughout the trajectory, although ArsC–arsenate complex was more stable compared to ChrR–Cr(VI) oxalate. Collectively, the Rg analysis suggested that the target proteins of strain PNPG3 maintain stable and compact conformations upon ligand binding, supporting their potential effectiveness in the biotransformation of heavy metals.

Water plays an important role in determining the structural organization, stability, and overall functionality of proteins. The SASA measures the extent of the protein surface that remains exposed to water molecules. A decrease in SASA generally reflects a more compact and stable protein–ligand complex, often resulting from the shielding of solvent-exposed residues, whereas elevated SASA values may indicate reduced folding or structural instability. As illustrated in Figure 7C, both complexes followed relatively linear trajectories and maintained stable profiles throughout the 100 ns simulation. The average SASA values for the ArsC–arsenate and ChrR–Cr(VI) oxalate complexes were 70.013 nm^2 and 99.890 nm^2, respectively. Notably, the SASA trends suggest that in both systems, the heavy-metal ligands initially interact near the outer regions of the binding pocket. Over time, they gradually migrate deeper into the binding cavity, engaging additional amino acid residues. This progressive inward movement enhances ligand–protein interactions and contributes to a reduction in solvent-exposed surface area, reflecting stable binding. Thus, the ArsC–arsenate complex displayed reduced solvent-accessible surface area, indicating a more compact and structurally stable interaction than the ChrR–Cr(VI) oxalate complex.

Hydrogen bonding is a critical determinant of the structural stability of biomolecular complexes. As depicted in Figure 7D, all examined protein–ligand systems formed multiple hydrogen bonds that remained dynamic, continuously forming and dissociating throughout the simulation, indicating stronger and more sustained stabilizing contacts within the binding pocket. These interactions substantially contribute to the observed binding affinities and favorable docking scores by reinforcing ligand accommodation within the active site.

Notably, the ArsC–arsenate complex demonstrated the highest hydrogen-bond occupancy, reaching a peak of five bonds. In contrast, the ChrR–Cr(VI) oxalate complexes displayed a maximum of four hydrogen bonds. This comparative trend indicated that arsenate binding to ArsC results in a more compact and structurally stable interaction profile, while the ChrR–Cr(VI) oxalate complex exhibited higher conformational variability, suggesting a relatively more flexible binding environment. The persistent turnover of these interactions underscores the inherently dynamic and adaptable nature of molecular contacts in biological environments. Consequently, the ArsC–arsenate complex exhibited higher hydrogen bond occupancy, indicative of a more compact and dynamically stable interaction compared with the ChrR–Cr(VI) oxalate complex.

Docking scores were therefore considered qualitative measures of relative binding preference rather than precise estimates of binding free energy. On this basis, arsenate emerged as the most favourably ranked ligand for ArsC, a trend that was consistently corroborated by MDS. The ArsC–arsenate complex displayed minimal RMSD, Rg, SASA values and reached structural equilibrium at an early stage of the simulation, indicative of a highly stable interaction. By contrast, within the ChrR system, the Cr(VI) oxalate complex showed the strongest docking preference and greater conformational stability relative to other ChrR–ligand combinations; nevertheless, it exhibited higher overall flexibility when compared with the ArsC–arsenate complex. Taken together, these findings underscore the preferential and dynamically robust association of arsenate with ArsC, while positioning the ChrR–Cr(VI) oxalate complex as a comparatively less stable complex. Given the higher stability of ArsC-arsenate, suggest that arsenate reduction may be more robust under fluctuating environmental conditions than Cr(VI) reduction, which aligns with the strong genomic enrichment in arsenic genes and the river Ganges arsenic context.

PCA

In the present study, the first two PCs were examined to evaluate dominant dynamic fluctuations and overall conformational variability. This observation of restricted motion was further substantiated by the high cumulative eigenvalue obtained from the diagonalized covariance matrix, which measured 67.05 nm² for the ArsC–arsenate complex, indicating more restricted and coherent atomic motions (Figure 7E). In contrast, the ChrR–Cr(VI) oxalate complex exhibited comparatively dispersed and less constrained movements, reflected by its substantially higher covariance value of 224.85 nm² (Figure 7E). This elevated value of ChrR-Cr(VI) oxalate suggests reduced structural rigidity and lower dynamic stability of ChrR–Cr(VI) oxalate complex throughout the simulation. In contrast, the ArsC–arsenate complexes displayed minimal conformational deviation, indicating that these systems remained near a stable equilibrium state, with only subtle, localized fluctuations observed over the course of the simulation. Accordingly, the ArsC–arsenate complex exhibited lower covariance, reflecting a more compact and structurally stable interaction than the ChrR–Cr(VI) oxalate complex. A comparable PCA performed by Alam and Saha demonstrated that the Azo-2–solvent black 3 and Azo-2–congo red complexes exhibited markedly greater structural stability than the Azo-1–solvent black 3 and Azo-1–congo red counterparts[7].

Conclusion

This study demonstrates a previously unreported convergence of highly efficient PNP biodegradation with pronounced tolerance to multiple toxic heavy metals in strain PNPG3, highlighting its exceptional adaptive capacity in chemically complex environments. The strain retained its catabolic efficiency under As stress, effectively degrading PNP with concomitant nitrite release. Genome annotation further confirmed the presence of a diverse repertoire of resistance genes associated with As, Cd, Co, and Cr detoxification, along with a well-organized atypical *arsRBHJ–GAPDH* gene cluster for As tolerance and biotransformation. These genomic attributes provide a mechanistic basis for the strain's resilience under mixed pollutant pressure. Complementary molecular docking and molecular dynamics simulations revealed that the protein–arsenate complex maintained high structural stability and compactness, indicating persistent interactions at the enzyme's active site. This *in silico* evidence is consistent with the observed phenotypic robustness of the strain in As-rich contexts. Collectively, these findings establish the strain's strong heavy-metal tolerance and biotransformation potential and underscore its promise for in situ bioremediation applications, which can be further evaluated through pilot-scale microcosm or column studies using authentic mixed-waste sediments. Future biochemical characterization of purified ArsC and ChrR proteins, including enzyme kinetics and metal reduction assays, will be essential to experimentally validate the computational predictions and to fully elucidate their functional roles in mixed contaminant resilience.

Limitations:

The present study has several limitations that should be acknowledged. Notably, experimental validation through enzyme kinetic assays was not performed, and the catalytic conversion of As(V) to As(III) or Cr(VI) to Cr(III) by purified proteins was not directly quantified. Consequently, the functional inferences regarding reductase activity are primarily derived from computational docking and MDS studies. While these *in silico* approaches provide valuable mechanistic insights into binding stability and interaction dynamics, they cannot fully substitute for biochemical evidence. Therefore, the conclusions should be interpreted with caution until corroborated by targeted in vitro or in vivo enzymatic assays.

Funding Statement

No funding is involved in this study.

Author contribution

SAA-Formal Analysis, designing of experiments, wet lab and docking, MDS Investigation, Methodology, Validation, and Writing, Review and Editing; PS-contributed reagents/materials, and reviewed drafts of the paper; DK- prepared heatmap, molecular docking; TN- initial wet lab experiment; RM, SB- reviewed drafts of the paper.

Ethics approval

This study does not require ethics approval

Conflict of Interest

The author claimed that there is no conflict of interest related to this work.

Consent for publication

This study does not require publication approval.

Data availability

The datasets generated and/or analysed during the current study are available in the Microbial Type Culture Collection and Gene Bank (MTCC), Institute of Microbial Technology (IMTECH), Chandigarh, India (accession number MTCC 13126), and in the National Center for Biotechnology Information (NCBI) repository, with raw sequencing reads deposited in the Sequence Read Archive under accession number SRR18163134 and the whole-genome shotgun sequence available under accession number JALLKV000000000.

Clinical trial number: not applicable

References

1. Abbas, S., Zulfiqar, S., Arshad, M., Khalid, N., Hussain, A., & Ahmed, I.. Molecular characterization of heavy metal-tolerant bacteria and their potential for bioremediation and plant growth promotion. *Front. Microbiol*, **16,** 1644466 (2025)
2. Akhter, M., Tasleem, M., Alam, M. M., & Ali, S. In silico approach for bioremediation of arsenic by structure prediction and docking studies of arsenite oxidase from *Pseudomonas stutzeri* TS44. *Int. Biodeterior. Biodegradation*, **122,** 82-91(2017).
3. Alam, S. A., & Saha, P. Biodegradation of p-nitrophenol by a member of the genus *Brachybacterium*, isolated from the river Ganges. *3 Biotech*, **12,** 1-10 (2022a)
4. Alam, S. A., & Saha, P. Evidence of *p*-nitrophenol biodegradation and study of genomic attributes from a newly isolated aquatic bacterium *Pseudomonas asiatica* strain PNPG3. *Soil Sediment Contam or Soil Sediment Contam. An Int. J.* **32,** 994-1011 (2022b).
5. Alam, S. A., & Saha, P. Chemotactic response of p-nitrophenol degrading *Pseudomonas asiatica* strain PNPG3 through phenotypic and genome sequence-based in silico studies. *3 Biotech*. **13**, 408. (2023).
6. Alam, S. A., Khan, B., Karmakar, D., Mandal, R., & Saha, P. Integrative bioinformatics and chemotactic insights into p-nitrophenol bioremediation by halotolerant aquatic *Pseudomonas* sp. strain PNPBRP5 (2). *Arch. Microbiol*, **207,** 1-12. (2025).
7. Alam, S. A., & Saha, P. Azoreductases of *Pseudomonas* sp. PNPG3: a bioinformatics and molecular simulation study for azo dye detoxification. *J Biomol Struct Dyn*. 1-17. (2025).
8. Altschul, S. F., Gish, W., Miller, W., Myers, E. W., & Lipman, D. J. Basic local alignment search tool. *J. Mol. Biol.* **215,** 403-410. (1990).
9. Artimo, P.,et al. ExPASy: SIB bioinformatics resource portal. *Nucleic Acids Res*, **40,** 597-603. (2012).
10. Arnold, K., Bordoli, L., Kopp, J., & Schwede, T. The SWISS-MODEL workspace: a web-based environment for protein structure homology modelling. *Bioinform.* **22**, 195-201. (2006).

11. Aziz, R. K., D. Bartels, A. A. Best, M. DeJongh, T. Disz, R. A. Edwards, K. Formsma, S. Gerdes, E. M. Glass, M. Kubal, et al. The RAST Server: rapid annotations using subsystems technology. *BMC Genom.* **9,** 75. (2008)
12. Fekih, I. B et al. Distribution of arsenic resistance genes in prokaryotes. *Front. Microbiol.* **9,** 2473. (2018).
13. Butcher, B. G., Deane, S. M., & Rawlings, D. E.. The chromosomal arsenic resistance genes of *Thiobacillus ferrooxidans* have an unusual arrangement and confer increased arsenic and antimony resistance to *Escherichia coli*. *Appl. Environ. Microbiol.* **66**, 1826-1833. (2000)
14. Chakraborti, D., et al. Groundwater arsenic contamination in the Ganga River Basin: a future health danger. *Int. J. Environ. Res. Public Health.* **15,** 180. (2018)
15. Colovos, C., and Yeates, & T. O. Verification of protein structures: patterns of nonbonded atomic interactions. *Protein Sci*. **2,** 1511-1519. (1993).
16. David, C. C., & Jacobs, D. J. Principal component analysis: a method for determining the essential dynamics of proteins. In *Protein dynamics: Methods and protocols* 193-226. Totowa, NJ: Humana Press. (2013)
17. DesMarias, T. L., & Costa, M. Mechanisms of chromium-induced toxicity. *Curr. Opin. Toxicol.* **14,** 1-7. (2019).
18. Geourjon, C., & Deleage, G. SOPMA: significant improvements in protein secondary structure prediction by consensus prediction from multiple alignments. *Bioinform.*, **11,** 681-684. (1995).
19. Genchi, G., Sinicropi, M. S., Lauria, G., Carocci, A., & Catalano, A. The effects of cadmium toxicity. *Int. J. Environ. Res. Public Health*, **17,** 3782. (2020).
20. Jaiswal, S., & Shukla, P.. Alternative strategies for microbial remediation of pollutants via synthetic biology. *Front. Microbiol*, **11,** 808 (2020)
21. Jan, A. T., Azam, M., Siddiqui, K., Ali, A., Choi, I., & Haq, Q. M. R. Heavy metals and human health: mechanistic insight into toxicity and counter defense system of antioxidants. *Int. J. Mol. Sci*. **16,** 29592-29630. (2015).
22. Jendele, L., Krivak, R., Skoda, P., Novotny, M., & Hoksza, D. PrankWeb: a web server for ligand binding site prediction and visualization. *Nucleic Acids Res*. **47,** 345-349. (2019).
23. Ji, G., & Silver, S. Regulation and expression of the arsenic resistance operon from Staphylococcus aureus plasmid pI258. *J. Bacteriol*. **174,** 3684-3694. (1992)
24. Khan, Z., Nisar, M. A., Hussain, S. Z., Arshad, M. N., & Rehman, A. Cadmium resistance mechanism in *Escherichia coli* P4 and its potential use to bioremediate environmental cadmium. *Appl. Microbiol. Biotechnol,* **99,** 10745-10757. (2015).
25. Klausen, M. S., Jespersen, M. C., Nielsen, H., Jensen, K. K., Jurtz, V. I., Soenderby, C. K., Sommer, M. O. A., Winther, O., Nielsen, M., Petersen, B & Marcatili, P. NetSurfP-2.0: Improved prediction of protein structural features by integrated deep learning. *Proteins: Struct., Funct., Bioinf*. **87,** 520-527. (2019).
26. Kuang S, et al. Effects of p-nitrophenol on enzyme activity, histology, and gene expression in *Larimichthys crocea*. *Comp. Biochem. Physiol. C Toxicol. Pharmacol.* **228,** 108638. (2020)
27. Laskowski, R. A., MacArthur, M. W., Moss, D. S., & Thornton, J. M. PROCHECK: a program to check the stereochemical quality of protein structures. *Appl. Crystallogr*. **26,** 283-291. (1993).

28. Laskowski, R. A., & Swindells, M. B. LigPlot+: multiple ligand–protein interaction diagrams for drug discovery. *J Chem Inf Model.* **51,** *2778-86* (2011).
29. Li, X., & Krumholz, L. R. Regulation of arsenate resistance in Desulfovibrio desulfuricans G20 by an arsRBCC operon and an arsC gene. *J. Bacteriol*. **189,** 3705-3711. (2007).
30. Liu, Y., Yang, X., Gan, J., Chen, S., Xiao, Z. X., & Cao, Y. CB-Dock2: improved protein–ligand blind docking by integrating cavity detection, docking and homologous template fitting. *Nucleic Acids Res*. **50,** 159-164. (2022)
31. Mitra, P., Singha, S., Roy, P., Saha, D., & Chatterjee, S. A molecular docking study between heavy metals and hydrophilic Hsp70 protein to explore binding pockets. *Journal of Proteins and Proteomics*, **15,** 413-428. (2024).
32. Moore, C. M., Gaballa, A., Hui, M., Ye, R. W., & Helmann, J. D. Genetic and physiological responses of *Bacillus subtilis* to metal ion stress. *Mol. Microbiol*. **57,** 27-40. (2005).
33. Neyt, C., Iriarte, M., Thi, V. H., & Cornelis, G. R. Virulence and arsenic resistance in Yersiniae. *J. Bacteriol,* **179,** 612-619. (1997).
34. Nurk, S., Meleshko, D., Korobeynikov, A., & Pevzner, P. A. metaSPAdes: a new versatile metagenomic assembler. *Genome Res*. *27*(5), 824-834. (2017).
35. Pellegrinetti, T. A., Monteiro, G. G. T. N., Lemos, L. N., dos Santos, R. A. C., Barros, A. G., & Mendes, L. W. PGPg_finder: a comprehensive and user-friendly pipeline for identifying plant growth-promoting genes in genomic and metagenomic data. *Rhizosphere*. **30,** 100905. (2024).
36. Rodrigues, C. S., A Aziz, S., Pereira, M. F. R., Soares, O. S. G. P., & Madeira, L. M. Degradation of p-Nitrophenol by activated persulfate with carbon-based materials. *J. Environ. Manage*, **343,** 118140. (2023)
37. Sengupta, K., Maiti, T. K., & Saha, P. Degradation of 4-nitrophenol in presence of heavy metals by a halotolerant *Bacillus* sp. strain BUPNP2, having plant growth promoting traits. *Symbiosis*, **65,** 157-163. (2015).
38. Sengupta, K., Swain, M. T., Livingstone, P. G., Whitworth, D. E., & Saha, P. Genome sequencing and comparative transcriptomics provide a holistic view of 4-nitrophenol degradation and concurrent fatty acid catabolism by *Rhodococcus* sp. strain BUPNP1. *Front. Microbiol.* **9,** 3209. (2019).
39. Stavrakakis, I., Remmas, N., Melidis, P., & Ntougias, S. Effect of the Oxidative Phosphorylation Uncoupler Para-Nitrophenol on the Activated Sludge Community Structure and Performance of a Submerged Membrane Bioreactor. *Water*, **13,** 3222. (2021).
40. Tasleem, M., El-Sayed, A. A. A., Hussein, W. M., & Alrehaily, A. Bioremediation of chromium-contaminated groundwater using chromate reductase from *Pseudomonas putida*: An in silico approach. *Water*, **15**, 150. (2022).
41. Tatusova, T., M. DiCuccio, A. Badretdin, V. Chetvernin, E. P. Nawrocki, L. Zaslavsky, A. Lomsadze, K. D. Pruitt, M. Borodovsky, & J. Ostell. NCBI prokaryotic genome annotation pipeline. *Nucleic Acids Res,* **44,** 6614-6624. (2016)
42. Tchieno, F. M. M., & Tonle, I. K. p-Nitrophenol determination and remediation: an overview. *Rev. Anal. Chem*, **37,** 20170019. (2018).
43. Tempestti, J. C. M., Mohan, H., Sathya, P. M., Lee, S. W., Venkatachalam, J., Oh, B. T., & Seralathan, K. K. Detoxification of p-nitrophenol (PNP) using *Enterococcus*

gallinarum JT-02 isolated from animal farm waste sludge. *Environ. Res*, **231,** 116289. (2023).
44. William, V. U., & Magpantay, H. D. Arsenic and microorganisms: genes, molecular mechanisms, and recent advances in microbial arsenic bioremediation. *Microorganisms*, **12,** 74. (2023).
45. White, G. F., Snape, J. R., & Nicklin, S. Biodegradation of glycerol trinitrate and pentaerythritol tetranitrate by *Agrobacterium radiobacter*. *Appl. Environ. Microbiol*. **62,** 637-642. (1996)
46. Wu, Y., Tepper, H. L., & Voth, G. A. Flexible simple point-charge water model with improved liquid-state properties. *J. Chem. Phys. 124*. (2006).
47. Yan, G., Chen, X., Du, S., Deng, Z., Wang, L., & Chen, S. Genetic mechanisms of arsenic detoxification and metabolism in bacteria. *Curr. Genet. 65*, 329-338. (2019).

Figure legends:

Figure 1: MIC assays for strain PNPG3 in presence of four heavy metals: (A) arsenite, (B) cadmium, (C) cobalt and (D) chromium.

Figure 2: (A) Biodegradation of PNP by strain PNPG3 in the presence of 1 mM arsenite, accompanied by the concurrent release of nitrite. (B) The growth response of strain PNPG3 on MM supplemented with PNP and 1 mM arsenite demonstrating visible decolorization, indicating effective degradation of PNP under metal-stress conditions.

Figure 3: Documentation of gene cluster organization of (A) strain PNPG3, (B) *Staphylococcus xylosus* pSX267, (C) *Thiobacillus ferrooxidans* Chr, (D) *Yersinia* pYV, and (E) *Ferroplasma acidarmanus* Chr, for comparative assessment of their functional content and genomic architecture

Figure 4. Heat map illustrating the comparative distribution of (A) stress-tolerance genes, (B) stress-associated biocontrol genes, (C) heavy-metal resistance determinants, and (D) xenobiotic detoxification genes across strain PNPG3, strain JS425, strain 13159349, strain WBC-3, and PNP.

Figure 5. Validation of the ArsC protein model using (A) the Ramachandran plot, (B) the QMEAN4 score, and (C) the ERRAT quality index, and the ChrR protein model through (D) the Ramachandran plot, (E) the QMEAN4 score, and (F) the ERRAT value.

Figure 6. Molecular docking analyses between PNPG3-derived receptors and their respective heavy-metal ligands: (A) ArsC–arsenate, (B) ArsC–arsenite, (C) ChrR–Cr(VI)carbonate, and (D) ChrR–Cr(VI) oxalate complexes. For each system, the left panel presents the predicted docking pose, while the right panel depicts the corresponding 2D interaction profile.

Figure 7. MDS of the ArsC–arsenate (black) and ChrR–Cr(VI) oxalate (red) complexes over a 100 ns trajectory. (A) The RMSF (B) Rg analysis reflects (C) The SASA plot (D) Hydrogen-bond profiles (E) PCA evaluation

Table 1: A BLASTX homology search for heavy-metal tolerance genes present in strain PNPG3

Table 2: Comparative analysis of heavy-metal tolerance gene homologs across multiple *Pseudomonas* strains.

Table 3: Comparative summary table of ArsC and ChrR for structural validation for model acceptance.

Table 4: The catalytic binding pocket characteristics of ArsC and ChrR prediction through the Prank web server.

Table 5: Binding free energy estimations for ligand interactions with ArsC and ChrR from strain PNPG3.

A

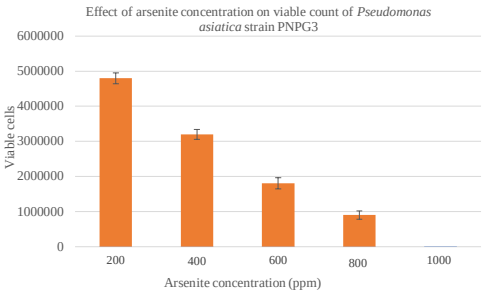

B

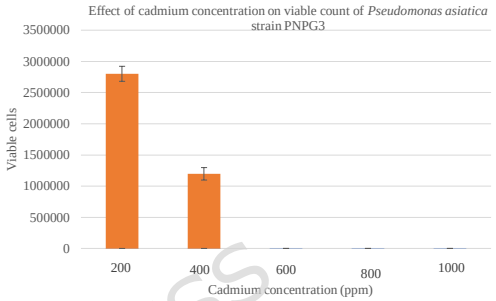

C

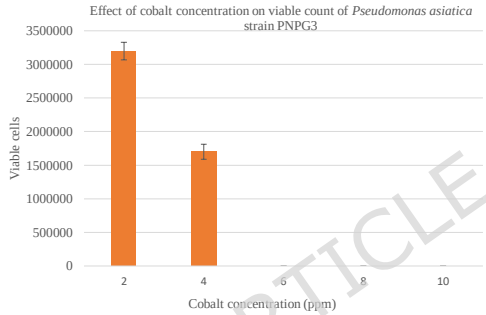

D

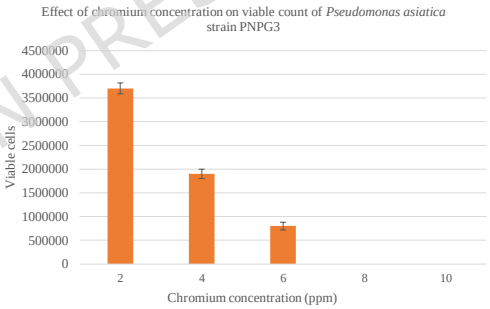

A

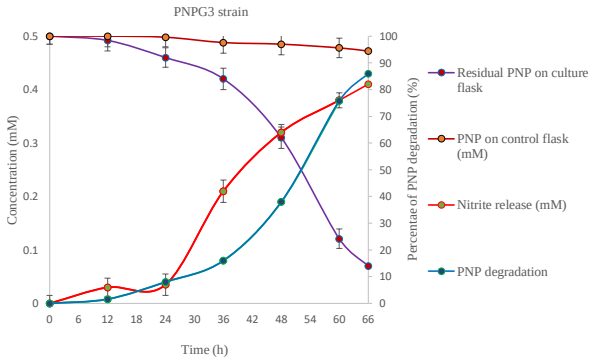

B

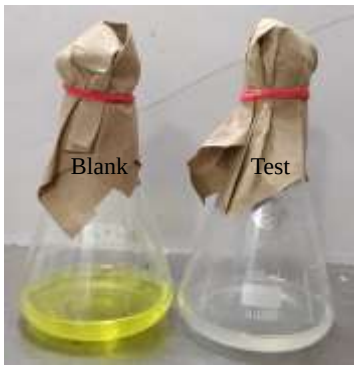

A

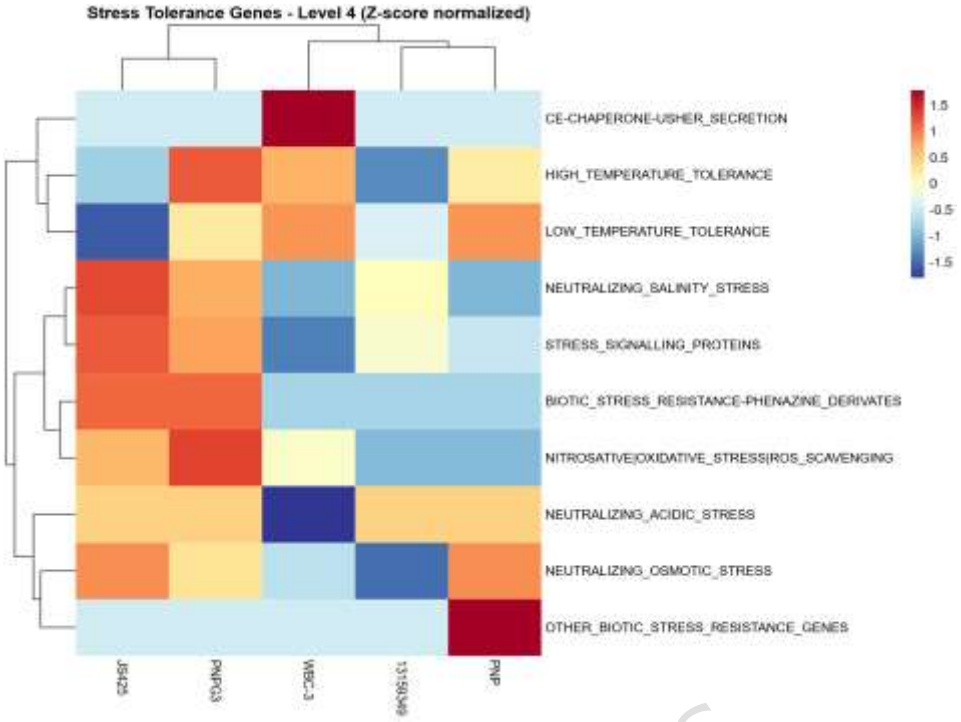

A

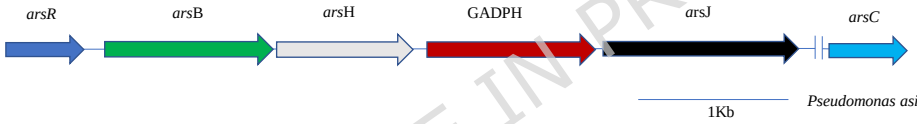

Pseudomonas asiatica strain PNPG3

B

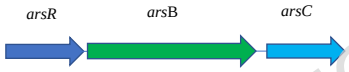

Staphylococcus xylosus pSX267; *Staphylococcus aureus* PI258; *Escherichia coli* Chr; *Pseudomonas aeruginosa* pKW301; *Pseudomonas fluorescens* Chr

C

Thiobacillus ferrooxidans Chr

D

Yersiniae pYV

E

Ferroplasma acidarmanus Chr

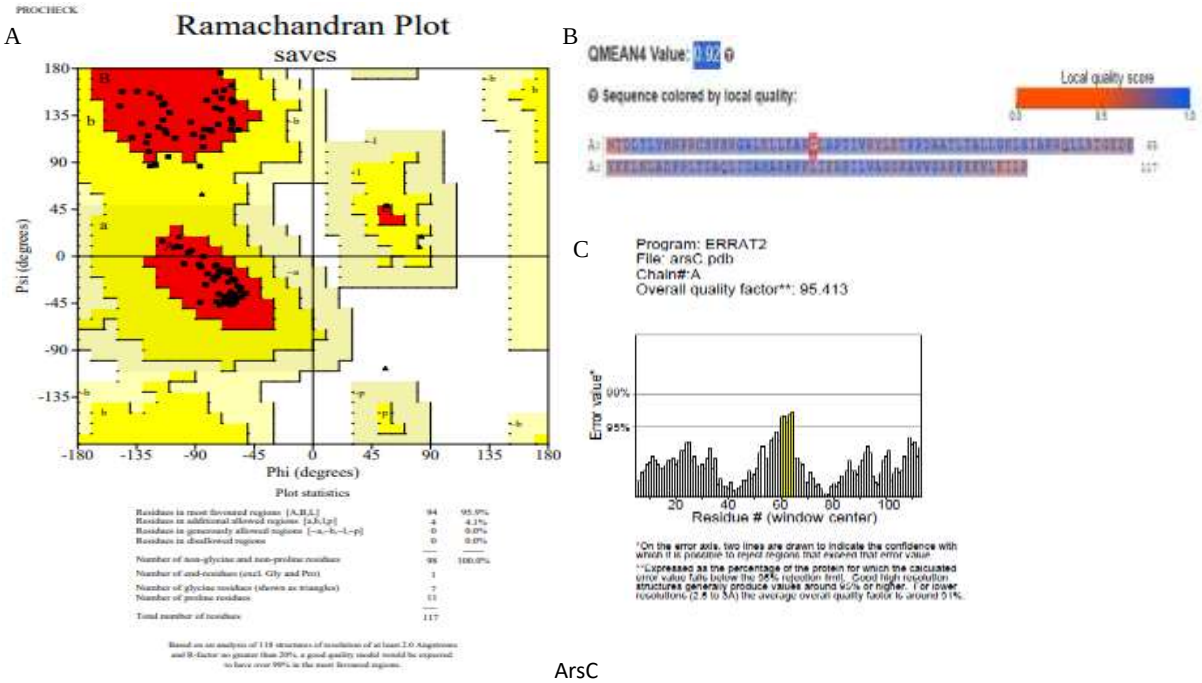

ArsC

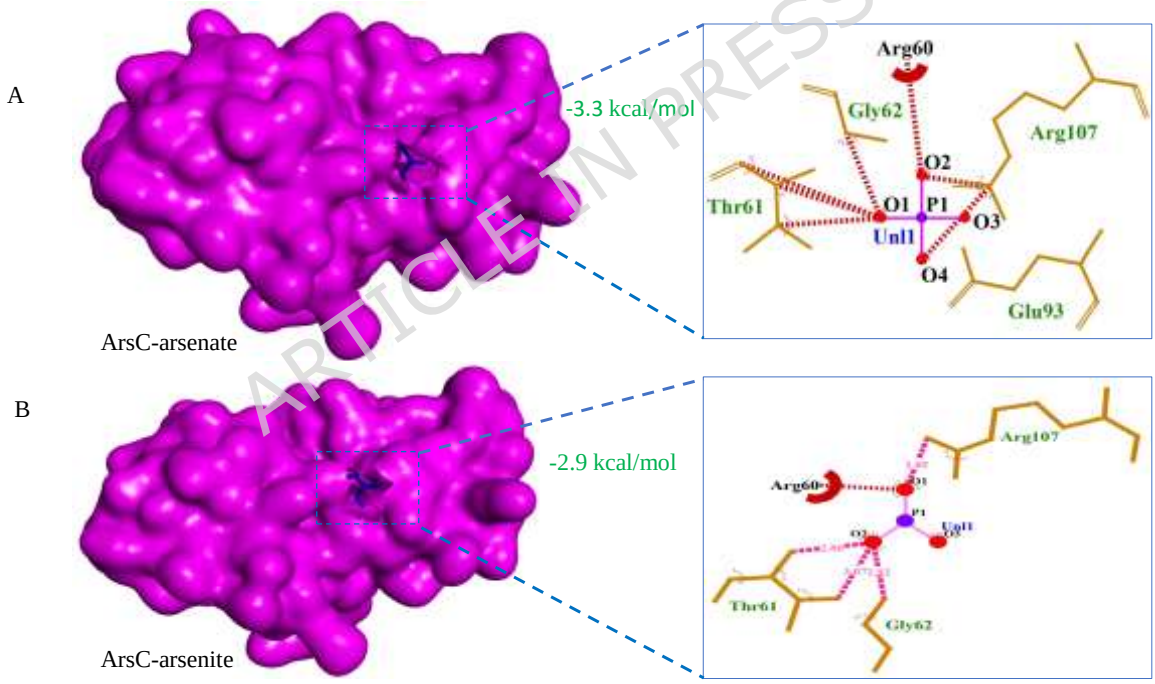

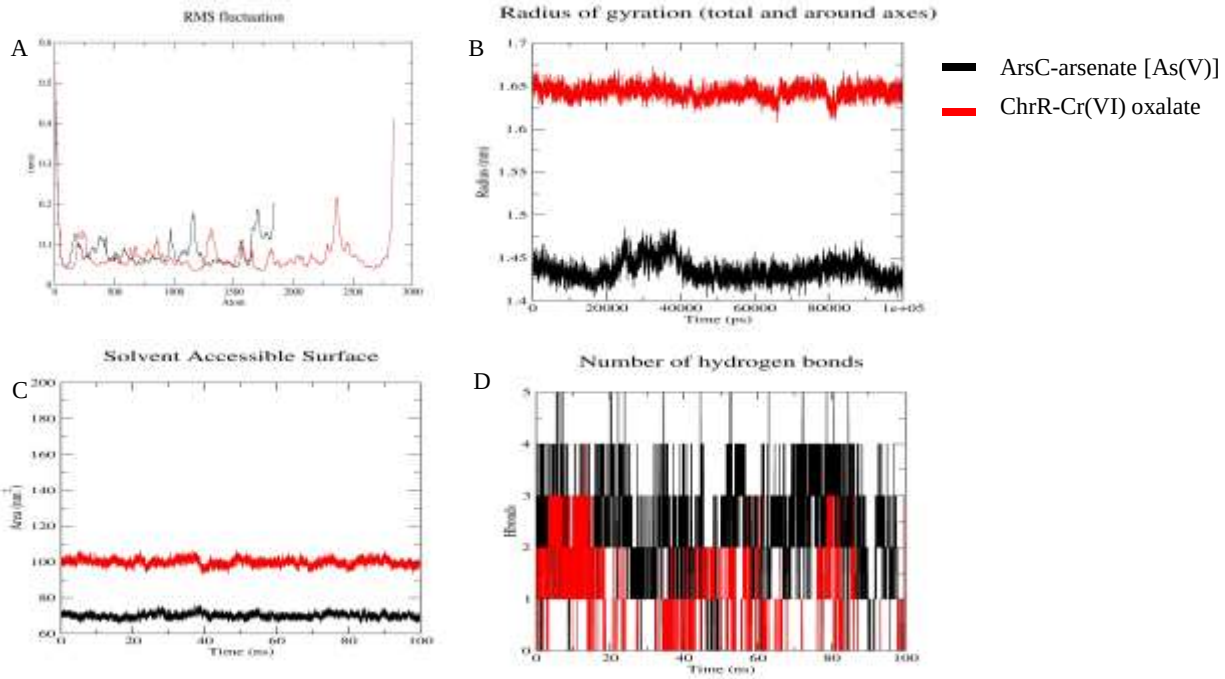

Table 1

Heavy Metal type	Locus tag PGAP; Protein ID	Function	Homology (%)	*E* value	Score	Origin (Accession no.)
Arsenic (As)	(MJ643_01555, JALLKV010000001); MCK2119281.1	metalloregulator ArsR/SmtB family transcription factor	100%	8e-80	241	*Pseudomonas* sp. (WP_013972227.1)
	(MJ643_01560, JALLKV010000001); MCK2119282.1	**ArsB,** ACR3 family arsenite efflux transporter,	100%	0.0	695	*Pseudomonas* sp. WP_013972226.1
	(MJ643_01565, JALLKV010000001); MCK2119283.1	**ArsH,** arsenical resistance protein ArsH,	100%	3e-176	494	*Pseudomonas* sp. WP_208209232.1
	(MJ643_01570, JALLKV010000001); MCK2119284.1	ArsJ-associated glyceraldehyde-3-phosphate dehydrogenase	100%	0.0	687	*Pseudomonas* sp. WP_013972224.1
	(MJ643_01575, JALLKV010000001); MCK2119285.1	**ArsJ,** organoarsenical effux MFS transporter ArsJ	100%	0.0	797	*Pseudomonas* sp. WP_013972223.1
	MJ643_06990 JALLKV010000007; MCK2120347	ArsR family transcriptional regulator	100%;	3e-152;	433	*Pseudomonas sp* (WP_013970739.1)
	(MJ643_13630, JALLKV010000017); MCK2121627.1	ArsC family reductase	100%	5e-79	239	*Pseudomonas plecoglossicida* (PBJ96712.1)
	(MJ643_19515, JALLKV010000032); MCK2122778.1	metalloregulator ArsR/SmtB family transcription factor	100%	0.0	659	*Pseudomonas* sp. WP_023661307.1)
	MJ643_20060 JALLKV010000034; MCK2122886	Arsenic resistance protein	100%;	7e-170;	484	*Pseudomonas sp* (WP_208209678.1)
	MJ643_20145 JALLKV010000034; MCK2122903	Arsenic transporter	100%;	0.0;	743	*Pseudomonas sp* (WP_208209673.1)
	(MJ643_27390, JALLKV010000069); MCK2124297.1	ArsC, arsenate reductase (glutaredoxin);	100%	1e-75	230	Pseudomonas sp (WP_047594822.1)
	(MJ643_29060, JALLKV010000085); MCK2124625.1	**ArsR** family transcriptional regulator	100%	2e-67	208	*Pseudomonas* sp. WP_003258229.1
Cadmium (cd)	(MJ643_05990, JALLKV010000005); MCK2120151.1	CadR, cadmium resistance transcriptional regulator	100%	3e-101	297	*Pseudomonas* sp. WP_015272183.1
	(MJ643_17445, JALLKV010000025); MCK2122372.1	CadA, cadmium-translocating P-type ATPase	100%	0.0	1415	*Pseudomonas* sp. WP_024087433.1

Table 2

Character	*Pseudomonas asiatica* strain PNPG3	*Pseudomonas putida* strain WBC-3	*Pseudomonas* sp. 13159349	*Pseudomonas* sp. JS425	*Pseudomonas alloputida* strain PNP
arsR	2	0	1	1	0
arsB	1	0	0	1	1
arsH	1	0	0	0	0
arsJ	1	0	0	1	1
arsC	1	0	1	0	1
cadR	1	1	2	0	2
cadA	1	0	0	3	3
chrA	1	0	0	0	1
chrR	1	0	0	1	1
cusA/***czcA*** family heavy metal efflux RND transporter	2	0	0	0	2
rcnB family gene	2	0	1	1	1

Table 3

Protein name	**ERRAT**	**Ramachandran Plot**	**QMEAN4**
ArsC	95.4128%	95.9% core region; 4.1% allowed region; 0.0% gener 0.0% disall	0.92
ChrR	97.1264%	94.3% core region; 5.7% allowed region; 0.0% gener 0.0% disall	-0.56
Cut off	50%	90%	<-4

Table 4: Prank web active site

Protein name	Score	Probablity	**Cavity volume ($Å^3$)**	Active site	Predicted active site
ArsC	5.52	0.278	188	Asn9, Arg11, Cys12, Ser13, Lys14, Leu35, Arg60, Glu63, Lys90, Arg94, Arg107	
ChrR	8.42	0.495	368	Ser13, Leu14, Arg15, Tyr19, Asn20, Pro79, Glu80, Tyr81, Ser116, Pro117,	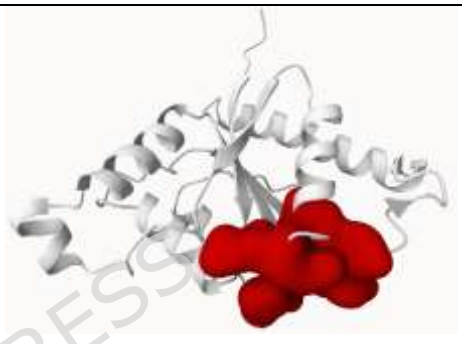

Table 5

Protein	Ligand (CID/SID no)	Docking score By CB-Dock2	Cavity volume ($Å^3$)	H bond	H bond distance (Å)	Interacting amino acids
ChrR	Cr(VI)_carbonate-21982989	-3.4kcal/mol	368	Ser13; Arg15; Asn20; Ser18; Ser19;	2.92; 3.08, 3.10; 3.05, 3.14; 2.94; 2.81;	SER13, ARG15 ASP17, SER18 TYR19, ASN20, ARG21, PRO79, GLU80, TYR81, ASN82, ARG83, VAL115, SER116, PRO117 GLY118, ILE120, GLY121, GLY122, PHE123, ALA151
ChrR	Cr(VI)-oxalate-129636852	-4.1kcal/mol	368	Ser13; Arg15; Ser18; Tyr19; Asn20;	2.88; 2.96; 2.91; 2.81; 3.05, 3.13;	SER13, ARG15 ASP17, SER18 TYR19, ASN20 ARG21, PRO79 GLU80, TYR81 ARG83, VAL115 SER116, PRO117 GLY118, ALA119 ILE120, GLY121 GLY122, PHE123 ALA151,
ArsC	Arsenite ion-544	-2.9kcal/mol	188	Thr61; Gly62; Arg107;	2.80, 3.07; 2.92; 2.85	ARG56, GLN57, LEU58, LEU59, ARG60, THR61, GLY62, GLU63, GLU93, VAL105, GLY106, ARG107, PRO108, LYS111
ArsC	Arsenate- 27401	-3.3 kcal/mol	188	-	-	ARG56, GLN57, LEU58, LEU59, ARG60, THR61, GLY62, GLU63, GLU93, VAL105, GLY106, ARG107, PRO108, LYS111